Table 1 Comparison of algorithms

Input data for generating test examples		Number of iterations for convergence of algorithm		
Geodetic latitude, deg	Altitudes, m	A	B	C
0.1	1, 10^3, 10^6	#, #, #	1, 2, 2	1, 1, 2
20	1, 10^3, 10^6	1, 2, 3	2, 3, 4	1, 1, 2
30	1, 10^3, 10^6	1, 2, 4	2, 3, 4	1, 1, 2
45	1, 10^3, 10^6	1, 2, 4	3, 4, 5	1, 1, 2
60	1, 10^3, 10^6	1, 2, 4	3, 4, 5	1, 1, 2
80	1, 10^3, 10^6	6, #, #	3, 4, 5	1, 1, 2
89.9	1, 10^3, 10^6	#, #, #	3, 4, 5	1, 1, 2

(14)] a_0, a_1, a_2, a_3, a_4 [see Eq. (13)], and initialize t_0 [see Eq. (16)], $k = 0$.

2. Set $k = k + 1$.

3. Compute t_k as a function of t_{k-1} [see Eq. (15)].

4. If $|(t_k - t_{k-1})/t_k| \leq \epsilon$, go to step 6; else, go to step 5.

5. If $k < k_{max}$, go to step 2; else, stop and write the message "Algorithm does not converge."

6. Determine $\tan^2\phi$ from Eq. (17).

7. Determine the geodetic latitude $\phi = \arctan(\tan\phi)$.

8. Compute altitude h from Eq. (18).

9. Compute geodetic longitude λ from Eq. (19).

Numerical Results

We now compare algorithms A and B, as described in Ref. 1, with the present algorithm C.

It is readily seen that the iterative parts of both algorithms A and C consist of updating the root of a fourth-degree polynomial by the Newton-Raphson method, and so they require the same number of arithmetical operations per iteration. Further, unlike algorithm B, algorithms A and C do not require square root evaluation in their iterative parts.

Algorithms A, B, and C were coded in FORTRAN in double precision and various examples were run. Some sample results are presented in Table 1. Assuming $\lambda = 0$ and using Eqs. (1-3), we generated data for test examples for three different altitudes, i.e., 1 m, 10^3 m, and 10^6 m, at each of the geodetic latitudes given in column 1 of Table 1. A slight change was made in the implementation of algorithms A and C, i.e., after each Newton-Raphson iteration of algorithms A and C, altitudes were also calculated. For a meaningful comparison, the same convergence criterion, i.e., the difference between the altitude obtained by a given algorithm and the altitude used to generate the corresponding test example is less than the given prescribed tolerance δ ($\delta = 10^{-5}$ m for Table 1), was applied to all three algorithms. In each row of column 3, three integers correspond to the iterations required for the convergence of algorithm A for test examples corresponding to 1 m, 10^3 m, and 10^6 m altitudes, respectively. In columns 4 and 5, the corresponding number of iterations for algorithms B and C are given. The symbol # denotes that the algorithm failed to converge in 10 iterations.

From Table 1 and other numerical results, the following observations were made:

1) For a given altitude, the iterations required for algorithms A and B depend on the geodetic latitude of the test example, whereas the iterations required for algorithm C do not vary with latitude.

2) Algorithm C has uniformly good performance from the equator to pole; algorithm B converges fast near the equator but its performance deteriorates steadily as we approach the pole; algorithm A has convergence problems near the equator as well as the pole.

3) For no test example did algorithm C require more iterations than algorithm A or B.

Thus, with its uniform good rate of convergence from the equator to pole, algorithm C is preferable to algorithms A and B.

Conclusions

The iterative algorithm developed in this Note is free from any singularity and has a uniformly good rate of convergence from the equator to pole and, hence, it can be considered for real-time applications requiring transformation from Earth-centered Earth-fixed coordinates to geodetic coordinates.

Remark

A polynomial of fourth degree $g(U)$ in $U = [(r + h)/a]^2$ was obtained by eliminating $t = r/a$ from Eqs. (11) and (12) of Ref. 1. Further, an iterative algorithm using the root of $g(U)$ was developed to transform ECEF coordinates to geodetic coordinates. However, algorithm C was found superior to this algorithm as well.

Acknowledgment

The author is thankful to Mr. M. N. Rao, Scientist E at the Defence Research and Development Laboratory, for his useful suggestions.

Reference

[1]Lupash, L.O., "A New Algorithm for the Computation of the Geodetic Coordinates as a Function of Earth Centered Earth Fixed Coordinates," *Journal of Guidance, Control, and Dynamics,* Vol. 8, Nov.-Dec. 1985, pp. 787-789.

Evaluation of Image Stability of a Precision Pointing Spacecraft

Hari B. Hablani*
Rockwell International, Seal Beach, California

Introduction

IN this Note, a device called the clutter leakage metrics, a Fourier integral form that is available in electro-optics literature, is presented in discrete Fourier transform terms. This device evaluates the image stability of a precision-pointing telescope. When a telescope undergoes severe vibrations, it may yield a cluttered image of a target. To minimize this clutter, electro-optic signals from successive frames are subtracted. Some clutter may still leak into the final image but then can be measured by the proposed metrics. These metrics involve the Fourier spectrum of pointing error, integration interval, and differencing operation. The metrics are illustrated for a telescope whose image stability during landmark tracking is disturbed by a neighboring solar array.

Clutter Leakage Metrics for a Telescope

When a telescope is articulated to a base body to which other deformable bodies are also attached, the environment of

Received July 15, 1985; revision received June 12, 1987. Copyright © American Institute of Aeronautics and Astronautics, Inc., 1987. All rights reserved.

*Member of the Technical Staff, Guidance and Control Group, Satellite Systems Division; Senior Member AIAA.

the telescope becomes rich in disturbances. If the pointing control system of the telescope cannot effectively reject these disturbances, the pointing error will exhibit high-frequency, sustained oscillations. Furthermore, for an infrared-sensitive telescope, the pixels are exposed to target radiance for a short time (measured in milliseconds) that is referred to as the integration interval. To obtain a smear-free image of the target, the telescope calculates the difference of successive signals from its focal plane. The traditional definition of image stability in terms of pointing error stability and stability rates does not systematically account for these inherent features of a telescope imaging system. On the other hand, electro-optics literature contains an estimate of clutter leakage in the Nth-differenced output of a pixel of a jittering telescope. Specifically, Rapier[1] has shown that if the jitter motion consists of a random root-mean-square amplitude $A = (A_x, A_y)$ at frequency ω, and if the integration interval is τ, then the Nth-differenced clutter leakage metric is given by

$$\Delta_N^2 = 2^{2N-1}A^2\,[\sin^{2N+2}(\omega\tau/2)]/(\omega\tau/2)^2 \tag{1}$$

For a precise definition of the integration interval, differencing operation, and clutter leakage, and a detailed formulation of Eq. (1), refer to Rapier[1]; for a condensed derivation of Eq. (1), see Ref. 2. For a continuous jitter spectrum that has the spectral density $P = (P_x, P_y)$, Rapier has further shown [see Eq. (27), Ref. 1] that

$$\Delta_N^2 = \frac{2^{2N}}{\pi}\int_0^\infty P(\omega)\,\frac{\sin^{2N+2}(\omega\tau/2)}{(\omega\tau/2)^2}\,d\omega \tag{2}$$

Equation (2) is obtained from Eq. (1) by applying the law of superposition, which is valid in the present context so long as the jitter spectrum is dominated by low-frequency components: $(\omega/2\pi) \ll 1/\tau$.

Telescopes are generally governed by a digital control system, so a discrete version of the integral in Eq. (2) is desired. For this purpose, let the discrete Fourier transform pair associated with the finite data string of the pointing error $\theta(\ell)$ be

$$\theta(\beta) = \frac{1}{L}\sum_{\ell=0}^{L-1}\theta(\ell)\,\exp\left(-i\,2\pi\,\frac{\beta}{L}\,\ell\right);$$

$$\theta(\ell) = \sum_{\beta=0}^{L-1}\theta(\beta)\,\exp\left(i\,2\pi\,\frac{\beta}{L}\,\ell\right) \tag{3}$$

where L = the total number of samples, an even number, and $\theta(\beta)$ is the discrete, complex Fourier transform. For computation purposes, it is more useful to have the following real sine transform version of Eq. (3):

$$\theta(\ell) = \theta(0) + \sum_{\beta=1}^{L/2-1} A(\beta)\,\sin[2\pi\,\beta\ell/L + \phi(\beta)]$$

$$+\,\theta(L/2)\cos\,\pi\ell \qquad (\ell = 0, \ldots, L-1) \tag{4}$$

where

$$A^2(\beta) \triangleq 4[\theta_R^2(\beta) + \theta_I^2(\beta)],\ \phi(\beta) \triangleq \tan^{-1}[-\theta_R(\beta)/\theta_I(\beta)] \tag{5}$$

The principle of superposition now can be applied to rewrite Eq. (2) for the position error in Eq. (4). The Δ_N^2 in the x- or y-coordinate then becomes

$$\Delta_N^2 = 2^{2N-1}\sum_{\beta=1}^{L/2-1} A^2(\beta)\,\frac{\sin^{2N+2}(\omega_\beta\tau/2)}{(\omega_\beta\tau/2)^2}$$

$$+\,2^{2N-1}\theta^2(L/2)\,\frac{\sin^{2N+2}(\omega_c\tau/2)}{(\omega_c\tau/2)^2} \tag{6}$$

where ω_c = half the sampling frequency, $\omega_\beta = 2\pi\beta/L\tau_s$ = the discrete frequency of a Fourier component, and $\tau_s \triangleq$ sample period of the telescope control system. Note that $\omega_c = \pi/\tau_s$ is the highest frequency that appears in Eqs. (4) or (6).

An Illustration and Discussion

The clutter leakage metrics, Eq. (6), for a three-body, precision-pointing, deformable spacecraft are illustrated in this section. The spacecraft consists of a central body $\mathcal{B}_0$, an elastic solar array $\mathcal{E}_1$ that has one rotational degree of freedom relative to $\mathcal{B}_0$, and a rigid, hard-mounted, pointing payload $\mathcal{B}_2$ that comprises a yoke and a telescope. The payload has two rotational degrees of freedom, intrack and crosstrack, relative to the central body and is designed to track landmarks. The intrack axis is collinear with the rotational axis of the solar array and pitch axis of the spacecraft, while the crosstrack axis lies in the roll-yaw plane. When the telescope is along the local vertical, the crosstrack axis is parallel to the roll axis of the spacecraft. Equations of motion for this spacecraft are derived in Ref. 2. The central body, the solar array, and the payload are each controlled independently. As usual, these control systems are designed on a single-axis basis that ignores the interaction between various bodies. However, with the aid of the clutter leakage metrics, it is shown below that the image stability of the telescope depends strongly on the flexibility and damping properties of the solar array and its control system. For this purpose, a digital simulation is developed that includes the motion equations of the deformable spacecraft in the form of vehicle modes, sampled nonlinear control systems of all the bodies, position and rate commands for the telescope, and several other important features.

The solar array's inertial orientation towards the sun is disturbed by the spacecraft's once-per-orbit rotation and the significant friction between the solar array and the central body. The steady state control torque T_{SA} that acts on the array at its hinge is a periodic, pulsating torque with a period τ_{SA} (10.4 sec) and frequency $f_{SA} = 1/\tau_{SA} = 0.096$ Hz. The exact profile of T_{SA} and its Fourier spectrum is shown in Ref. 2. The recurrent torque T_{SA} induces sustained excitation mostly of a torsional mode of the solar array at the frequency 2.33 Hz. This mode is the third-vehicle elastic mode. On the other hand, although the reaction torque $-T_{SA}$ acts on the central body about the pitch axis, owing to significant inertial coupling between the roll and pitch axes, the attitude angles and rates about both axes are excited. Furthermore, the inertial rate commands expressed in the telescope frame for tracking a landmark use the attitude angles and rates of the base body; see the command equations in Ref. 3. Consequently, the vibrations of the base body, attenuated through

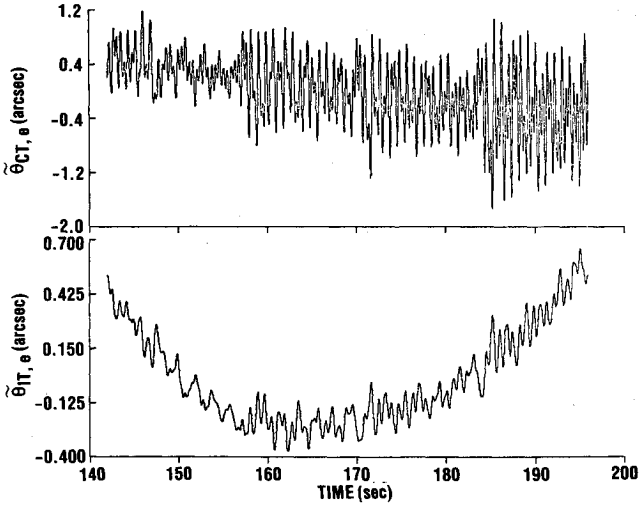

Fig. 1 Oscillatory part of true position errors: flexible spacecraft, $\zeta = 0.1\%$.

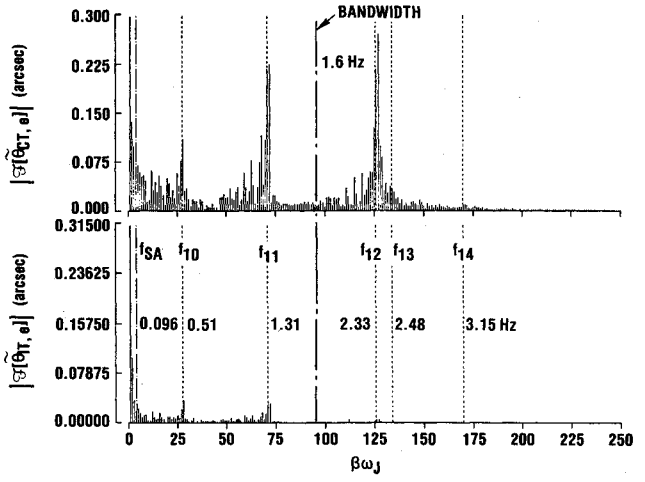

Fig. 2 Fourier spectrum of true position errors: flexible spacecraft, $\zeta = 0.1\%$.

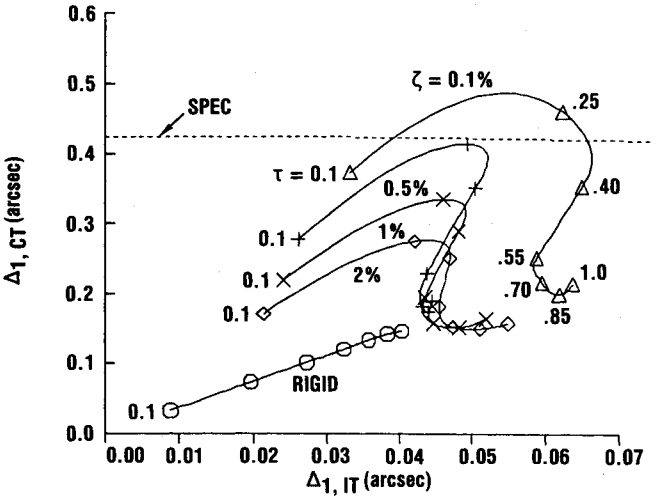

Fig. 3 Dependence of the first clutter leakage metrics on frame time and damping.

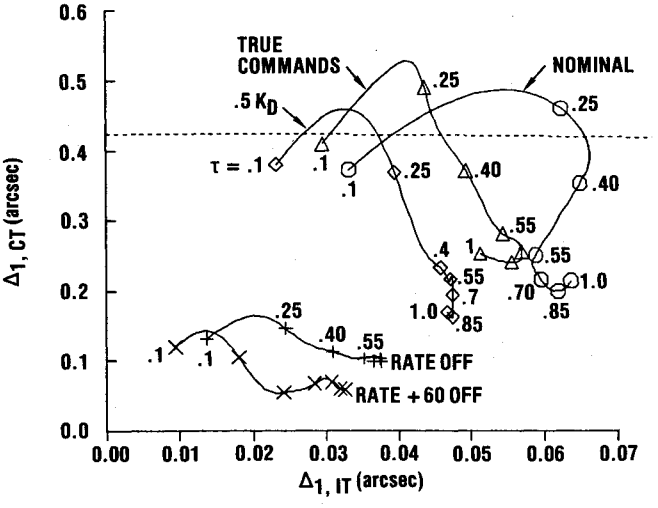

Fig. 4 Clutter leakage metrics in four experimental commands.

the characteristics of the telescope pointing controller, manifest themselves in the pointing errors about intrack and crosstrack axes. The pointing controllers for both axes are almost identical; the control system for the tracking phase of pointing is a Type 3 system and has a bandwidth of 1.6 Hz (Ref. 3). With this controller. Fig. 1 furnishes an example of the true position errors $\tilde{\theta}_{IT,e}$ and $\tilde{\theta}_{CT,e}$ of the telescope's line-of-sight; the nonzero means of these errors have already been subtracted. The above subscripts *IT* and *CT* mean intrack and crosstrack. These errors are labeled true because they are based on true control commands that are free from the errors caused by command extrapolation and by the age of the carrier body $\mathcal{B}_0$ sampled attitude angles and rates. The actual control commands used by the control systems in the simulation are not free from these errors. Figure 1 indicates that $\tilde{\theta}_{CT,e}$ is nearly an order of magnitude larger than $\tilde{\theta}_{IT,e}$. This is explained as follows. Recall that the solar array is free to rotate about the pitch axis and constrained in the roll-yaw plane. Therefore, for the first four vehicle modes in which transverse and in-plane bending and torsion of the solar array predominates over those of other components and for a certain orientation of the solar array, the roll modal coefficients are nearly eight times larger than the pitch modal coefficients. Also recall that the intrack and pitch axes are collinear, while the crosstrack axis is in the roll-yaw plane. Furthermore, it is shown in Ref. 3 that the crosstrack mean acceleration command is 5.7 times its intrack counterpart. Consequently, the amplitude and frequency content of the crosstrack error is significantly higher than those of the intrack error. Precisely this is seen in Fig. 2, which portrays the fast Fourier transform of the errors in Fig. 1. If τ_j is the time span of the errors portrayed in Fig. 1 (currently 60 s), then let $\omega_j = 2\pi/\tau_j$ (0.105 rad/s = 0.0167 Hz). The abscissa in Fig. 2 is an integer multiple of ω_j. Sustained excitation of the first three elastic modes in crosstrack, particularly the second and the third modes, is evident in Fig. 2. In intrack, the contribution of the elastic modes to the error is relatively negligible.

Knowing the fast Fourier transform of the errors, that is, the amplitudes $A(\beta)$ and the frequency ω_β ($\beta = 1, \ldots, L/2$) in Eq. (6) for the two degrees of freedom of the telescope, we now compute the clutter metric $\Delta_N (N = 1, \ldots)$. Figure 3 shows the relationships between $\Delta_{1,IT}$ and $\Delta_{1,CT}$, with τ as a parameter and the equivalent viscous damping ζ in elastic modes equal to 0.1, 0.5, 1.0, and 2.0 percent. The jitter metrics are computed for 91 values of τ, with $\tau = 0.10, 0.11, \ldots, 1.0$ s. The metrics of Δ_1 for a rigid spacecraft are also shown in Fig. 3. It can be seen that the metrics depend strongly on the frame integration interval τ. For a flexible spacecraft, they first increase with τ and reach a summit around $\tau =$ 0.25 s; the trend then gradually reverses, and the metrics start decreasing with τ at a slow rate, reaching a trough around 0.6 or 0.7 s. After that, a slight increase in the metrics takes place until $\tau = 1.0$ s. The range of $\tau > 1.0$ s is not of much practical use for infrared sensors. With damping, the metrics decrease because as damping increases the peaks of the position error amplitudes are diminished. For the current telescope, the specification arc is shown by a dashed line in Fig. 3. Whether or not specifications are met depends on the damping coefficient and the frame time τ. Finally, the rigid spacecraft has very low jitter metrics that increase monotonically with τ and always stay much lower than those of flexible spacecraft.

It is desirable that the clutter leakage metrics be low, so those corresponding to four experiments are displayed in Fig. 4. For comparison, the jitter metrics corresponding to the nominal system with $\zeta = 0.1$ percent are also shown in Fig. 4. In the first experiment, the gain of the solar array drive K_D is halved, and the corresponding leakage metrics curve is labeled "0.5 K_D." By halving the gain, the metric Δ_1 decreases and almost always meets the specification. In the second and third experiments, the solar array controller is turned off as soon as the telescope enters the precision tracking mode and 60 seconds before it enters that mode, respectively. In Fig. 4, the corresponding curves are labeled "Rate Off" and "Rate + 60 Off," respectively. The jitter metrics plummet from their nominal values to values that are far below the specified limits. Thus, if the telescope is found to jitter unacceptably during flight, a viable solution is to turn off the solar array controller. Lastly, in Fig. 4 the results of the fourth experiment, in which true rate commands are used, are labeled

"True Commands," and the corresponding jitter metrics are clearly smaller than the nominal values.

Conclusions

The clutter leakage metrics for the measurement of telescope image stability illustrated in this paper are quite valuable, particularly when the telescope undergoes the significant vibrations caused by an adjacent, deformable, articulated body such as a solar array or by control actuators such as reaction wheels or control-moment gyros. In these circumstances, since the Fourier spectrum of the telescope's pointing error is wide, the conventional method of measuring pointing accuracy in terms of stability and stability rates is inadequate. In the numerical example considered, the leakage metric is high for low damping of the solar array, which implies that greater damping yields a better image. Furthermore, the metric depends heavily upon the integration interval; below a certain limit, the smaller the interval, the better the image. The numerical illustration, therefore, also exemplifies control-structure and payload-to-payload interaction.

References

[1]Rapier, J.L., "Clutter Leakage Approximations for Staring Mosaic Senors with Simultaneous LOS Drift and Jitter," Paper 253-32, 24th Technical Symposium, Society of Photo-Optical Instrumentation Engineers, San Diego, CA, July 1980.

[2]Hablani, H. B., "Dynamics of a Deformable Pointing Spacecraft by Kane's Method, and Telescope's Image Stability Evaluation," *Proceedings of the AIAA Guidance, Navigation, and Control Conference,* New York, Aug. 1986, pp. 644-56.

[3]Hablani, H. B., "Design of a Spacecraft Pointing Control System for Tracking Moving Objects," AIAA Paper 87-2597, Aug. 1987.

Principal Coordinate Realization of State Estimation and Its Application to Order Reduction

Yoshikazu Miyazawa* and Earl H. Dowell†
Duke University, Durham, North Carolina

I. Introduction

MODELING of plant dynamics is an important problem, especially when designing a time-invariant optimal estimator. Since the optimal estimator is generally of the same order as the plant dynamics, the estimator becomes of high order if the plant is modeled accurately with a high-order system.[1] In practice, however, such full-state estimation is often useless, and some sort of order reduction is possible and necessary.[2] For the fixed-order optimal estimator problem, optimality conditions and a computational algorithm have been discussed in Refs. 3 and 4. In order to make the iterative algorithm converge to the global minimum, an appropriate initial solution, or a suboptimal reduced-order estimator, is necessary. Furthermore, a quantitative index for measuring the accuracy of the order reduction is desirable.

This note proposes that a set of singular values be used as an quantitative index that shows estimation accuracy in terms of the state components. Such an approach introduces a unique realization of the plant model and the estimator. Since the singular values show not only estimation quality but also coupling intensities of each state, a principal coordinate realization can be used for the derivation of a reduced-order (or simplified) estimator. The proposed reduced-order estimator does not claim any optimality, nor guarantee better performance than other methods. However, with only a small computational demand, it gives reasonable results, especially when the system has several small singular values.

II. System Description and Principal Coordinate Realization

The plant dynamics is given by the following state equation:

$$dx/dt = Ax(t) + Bw(t)$$

$$y(t) = Cx(t) + v(t), \qquad \eta(t) = Dx(t) \tag{1}$$

$x \in R^n$ is the state $y \in R^m$ is the measurement. $\eta \in R^q$ is a variable to be estimated from the measurement y. $w \in R^p$ and $v \in R^m$ are plant disturbance and measurement noise, respectively. It is assumed that they are Gaussian white noise and their stochastic characteristics are given by

$$E\begin{bmatrix} w(t) \\ v(t) \end{bmatrix} = 0, E\left[\begin{pmatrix} w(t) \\ v(t) \end{pmatrix}[w(t+\tau)^T, v(t+\tau)^T]\right] = \begin{bmatrix} W, W_v \\ W_v^T, V \end{bmatrix}\delta(\tau) \tag{2}$$

where W and V are positive-definite.

It is assumed that (A,B) is controllable, (C,A) is observable, and the system is asymptoticaly stable. The full-order optimal estimator is given by

$$d\hat{x}/dt = A\hat{x}(t) + K[y(t) - C\hat{x}(t)], \qquad \hat{\eta}(t) = D\hat{x}(t)$$

$$K = (XC^T + BW_v)V^{-1} \tag{3}$$

$\hat{\eta}$ is the estimated value for η. The covariance matrix of the error is X, i.e.,

$$E[ee^T] = X, \qquad e(t) = \hat{x}(t) - x(t) \tag{4}$$

It satisfies the following Riccati equation:

$$AX + XA^T + BWB^T - (XC^T + BW_v) \times V^{-1}(XC^T + BW_v)^T = 0 \tag{5}$$

The covariance matrices of the state and its estimate are defined as

$$E[xx^T] = X_1, \qquad E[\hat{x}\hat{x}^T] = X_2 \tag{6}$$

They satisfy the following:

$$AX_1 + X_1A^T + BWB^T = 0, \qquad X_2 = X_1 - X \tag{7}$$

Under the assumptions of controllability and observability, the three covariance matrices are positive-definite, i.e., X_1, X_2, $X > 0$.

When the state transformation $\xi = Tx$ is carried out, the dynamics of the estimator are not changed, and it can be rewritten in terms of the transformed system matrices $(TAT^{-1}, TB, CT^{-1}, DT^{-1})$. If we consider the transformed covariance matrices of three variables x, $\hat{x}$, and e, there exists

Received Jan. 14, 1987. Copyright © American Institute of Aeronautics and Astronautics, Inc., 1987. All rights reserved.

*Visiting Scholar, Department of Mechanical Engineering and Materials Science, on leave from the National Aerospace Laboratory, Japan. Member AIAA.

†Dean, School of Engineering. Fellow AIAA.